2D Perovskite $Sr_2Nb_3O_{10}$ for High-Performance UV Photodetectors

Siyuan Li, Yong Zhang, Wei Yang, Hui Liu, and Xiaosheng Fang*

2D perovskites, due to their unique properties and reduced dimension, are promising candidates for future optoelectronic devices. However, the development of stable and nontoxic 2D wide-bandgap perovskites remains a challenge. 2D all-inorganic perovskite $Sr_2Nb_3O_{10}$ (SNO) nanosheets with thicknesses down to 1.8 nm are synthesized by liquid exfoliation, and for the first time, UV photodetectors (PDs) based on individual few-layer SNO sheets are investigated. The SNO sheet-based PDs exhibit excellent UV detecting performance (narrowband responsivity = 1214 A W^{-1}, external quantum efficiency = 5.6×10^5%, detectivity = 1.4×10^{14} Jones @270 nm, 1 V bias), and fast response speed ($t_{rise} \approx 0.4$ ms, $t_{decay} \approx 40$ ms), outperforming most reported individual 2D sheet-based UV PDs. Furthermore, the carrier transport properties of SNO and the performance of SNO-based phototransistors are successfully controlled by gate voltage. More intriguingly, the photodetecting performance and carrier transport properties of SNO sheets are dependent on their thickness. In addition, flexible and transparent PDs with high mechanical stability are easily fabricated based on SNO nanosheet film. This work sheds light on the development of high-performance optoelectronics based on low-dimensional wide-bandgap perovskites in the future.

For decades, substantial progress in high-performance photodetectors (PDs) has opened unprecedented possibilities for technological advances, among which UV PDs based on wide-bandgap semiconductors are a crucial component for diverse applications, such as spectral analysis, environment monitoring, and optoelectronic devices.[1–4] To meet the requirements of next-generation high-performance PDs, including energy-efficient, miniaturized, and flexible applications, 2D materials are considered promising candidates to address the challenges.[5] Among them, 2D perovskites have attracted increasing research interest and been applied to diverse fields, such as light-emitting diodes (LEDs), solar cells, and PDs, because of the advantages peculiar to them.[6–8] First, inherited from their bulk counterparts and originated from

their reduced dimension, 2D perovskites exhibit a variety of intriguing properties, including tunable bandgap, high photoconductive gain, high photoluminescence (PL) efficiency, and nonlinear optical properties.[6,8–10] Second, it is found that many properties of 2D perovskites are strongly dependent on their thickness, and the properties show increased sensitivity to applied external fields owing to their ultrathin thickness.[11–13] Next, 2D materials are considered as ideal building blocks for constructing complex nanoarchitectures, such as van der Waals heterostructures and superlattices, leaving room for novel material design and engineering.[14,15] 2D perovskites also exist as an excellent platform for chemical modification to meet practical needs.[16–18] Besides, like other 2D materials, 2D perovskites are promising candidates for transparent and flexible optoelectronic devices, due to their excellent mechanical properties and ultrathin thickness.[19] Despite the advantages mentioned above, the environmental instability and the presence of the toxic element Pb in high-performance perovskites remain two major challenges.[20] And the narrow bandgap of most 2D perovskites hinders their application in high-performance visible–blind UVB or even UVC PDs. Therefore, it is still in need to develop stable and nontoxic 2D wide-bandgap perovskites to tackle those issues.

2D perovskite strontium niobate ($Sr_2Nb_3O_{10}$, SNO), exfoliated from Dion–Jacobson layered oxide $KSr_2Nb_3O_{10}$ or $CsSr_2Nb_3O_{10}$, has attracted increasing research interest due to its unique structure and properties.[21,22] In the family of transition-metal-oxide perovskites, a host of novel properties have been discovered owing to strongly interacting d orbital electrons.[23,24] For instance, previous studies explored the high catalytic performance of $H[M_2Nb_3O_{10}]$ (M = Ca, Sr) perovskite family toward hydrogen evolution, in which their unique layered structure provides abundant active sites and promotes reactant migration.[16,25] Domen et al. discovered that among the $H[M_{n-1}Nb_nO_{3n+1}]$ (n = 2, 3, 4) family, $HSr_2Nb_3O_{10}$ exhibits the highest photocatalytic activity for water splitting, and the performance could be further enhanced by loading Pt.[26] Moreover, exfoliated SNO nanosheets are proven to be a thermally stable ultrathin dielectric material with high dielectric constant outperforming various perovskite thin films such as $(Ba_{1-x}Sr_x)TiO_3$.[21,22] Besides, the ferroelectric properties of SNO have

S. Y. Li, Dr. Y. Zhang, W. Yang, Dr. H. Liu, Prof. X. S. Fang
Department of Materials Science
Fudan University
Shanghai 200433, P. R. China
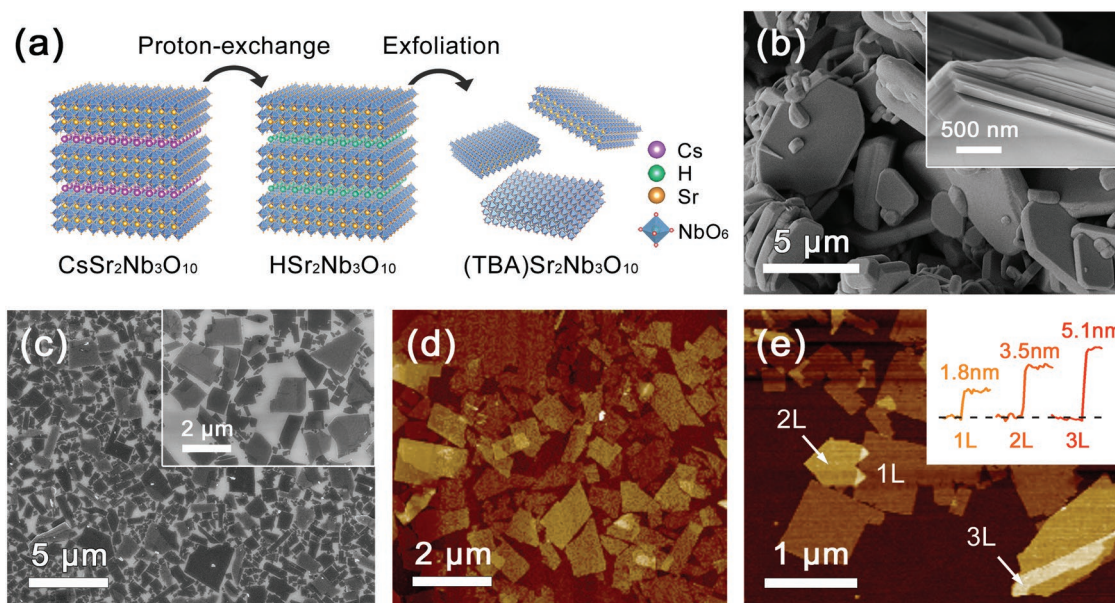E-mail: xshfang@fudan.edu.cn

Figure 1. a) The schematic illustration of the preparation process of SNO nanosheets via proton-exchange and exfoliation processes from bulk precursor CSNO. b) The SEM image of obtained CSNO precursor after calcination, the inset showing the layered nature of CSNO grains. c) The SEM image of SNO nanosheets after exfoliation, with the inset at higher magnification. d,e) The AFM images of SNO nanosheets dispersed on a silicon substrate. The corresponding height profiles of 1L, 2L, and 3L SNO nanosheets are shown in the inset.

been investigated after alkylamine intercalation.[27] All these intriguing properties above, as well as its stable and nontoxic nature, make SNO a promising candidate for broader applications. It is noticed that SNO has a wide bandgap corresponding to UV photon energy,[23] offering possibilities for constructing high-performance visible–blind UV PDs based on exfoliated SNO nanosheets. However, compared with the properties mentioned above, little attention has been paid to the photoresponsive properties of SNO,[28] let alone systematic investigation on UV PDs based on individual SNO nanosheets.

Herein, 2D all-inorganic perovskite SNO nanosheets with thicknesses down to 1.8 nm are synthesized by high-temperature solid-state reaction and liquid exfoliation. The layered morphology, crystallinity, and optical and photoluminescent properties are characterized by multiple characterization methods. For the first time, UV PDs based on individual few-layer SNO sheets are fabricated, on the basis of which the photodetecting performance of SNO is systematically investigated. The SNO sheet–based PDs exhibit excellent performance, including outstanding responsivity, external quantum efficiency (EQE), and fast response speed, outperforming most of reported 2D material–based UV PDs. Furthermore, by applying gate voltage, the carrier transport properties of SNO and the performance of SNO-based phototransistors are also investigated. More importantly, based on individual SNO nanosheets with various thicknesses, we investigate the thickness dependence of photodetecting performance and carrier transport properties. In addition, we further report a successful attempt for the easy fabrication of flexible and transparent PDs based on SNO nanosheet film. This work sheds light on the development of high-performance optoelectronics based on stable low-dimensional wide-bandgap perovskites in the future.

The schematic illustration of the preparation process of SNO nanosheets and the morphologies of the obtained products are shown in **Figure 1** and Figure S1 (Supporting Information), respectively. Briefly, SNO nanosheets are prepared via a two-step high-temperature solid state reaction (calcination), proton-exchange in hydrochloric acid, and subsequent exfoliation in tetrabutylammonium (TBAOH) aqueous solution. After calcination, $CsSr_2Nb_3O_{10}$ (denoted as CSNO) precursor with lateral grain size in micrometer scale is confirmed by scanning electron microscopy (SEM) to possess a layered nature (Figure 1b), leaving room for subsequent intercalation and exfoliation. And micrometer-sized SNO nanosheets are successfully prepared by exfoliating protonic $HSr_2Nb_3O_{10}$ (HSNO) sample. Based on the statistic results in Figure S2a (Supporting Information), the median lateral size of SNO nanosheets is determined to be 0.9 µm. Furthermore, the atomic force microscopy (AFM) method is utilized to characterize the thickness of exfoliated SNO nanosheets. According to the height profiles, the thickness of exfoliated single-layer (1L), 2L, and 3L SNO sheets are measured as 1.8, 3.5, and 5.1 nm, respectively. Based on the thickness distribution in Figure S2b (Supporting Information), the thickness values statistically cluster around several discrete numbers, further suggesting the layered nature of SNO. By fitting the thickness data, the relationship between the thickness and layer number could be determined as $t = 1.71n$, where t is the nanosheet thickness and n stands for the layer number. The measured layer thickness of SNO is consistent with previous reports (1.73 nm).[23]

To determine the crystal phase evolution during the preparation process, the X-ray powder diffraction (XRD) method is conducted for bulk samples after calcination and proton exchange, with the grazing incidence XRD (GIXRD) conducted for SNO nanosheets due to their ultrathin thickness. The XRD pattern of
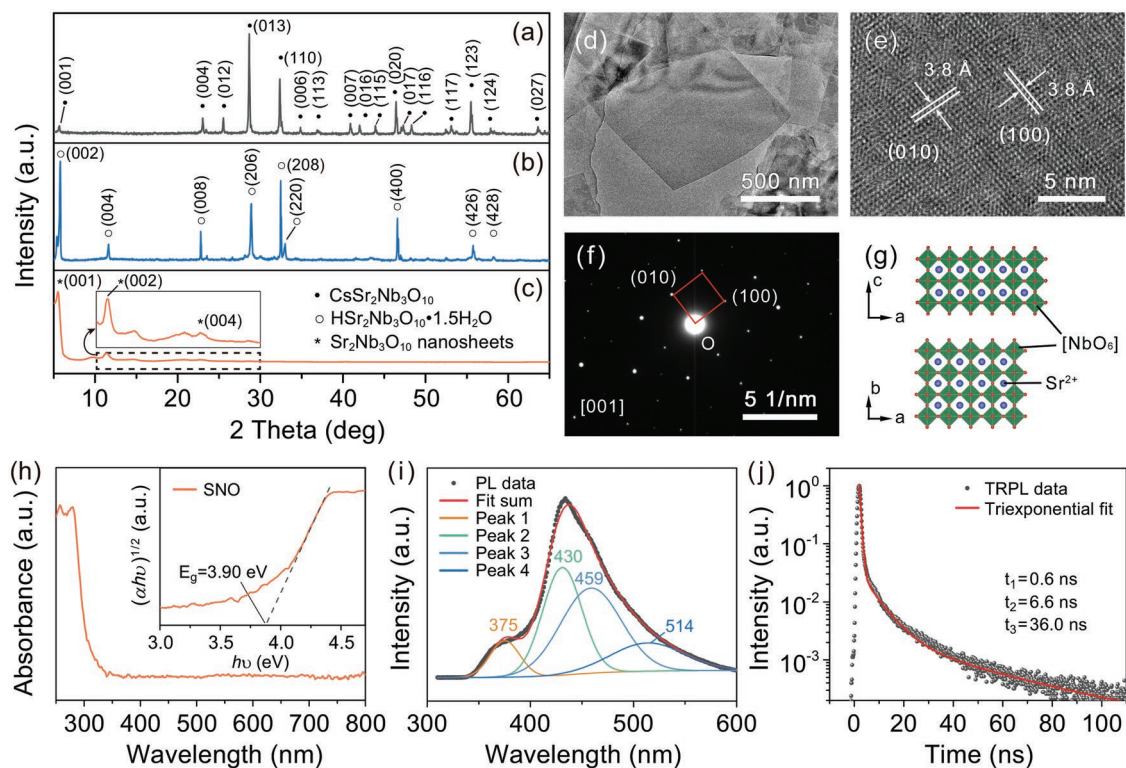
Figure 2. The XRD patterns of samples after a) calcination and b) proton exchange, and c) GIXRD pattern of exfoliated nanosheets. The d) TEM and e) HRTEM images of SNO nanosheets. f) The SAED pattern along the [001] zone axis. g) Schematic illustration for the crystal structure of SNO. h) UV–vis absorption spectrum of SNO, with the corresponding Tauc curve in the inset. i) The Gaussian-fitted room-temperature PL emission spectrum, with an excitation wavelength of 300 nm. j) The TRPL spectrum of SNO.

powder synthesized by calcination (**Figure 2**a) matches well with the standard data of $CsSr_2Nb_3O_{10}$ (PDF#53-1047), with the three highest peaks at 28.6°, 32.4°, and 46.4° corresponding with (013), (110), and (020) planes. After the proton-exchange process, the three highest peaks located at 5.7°, 28.5°, and 32.1° correspond to (002), (206), and (208) planes of $HSr_2Nb_3O_{10} \cdot 1.5H_2O$ (PDF#51-1878), suggesting a successful replacement of Cs^+ with H^+. Furthermore, after the TBA^+-assisted exfoliation process, the GIXRD pattern of SNO sheets exhibits obvious peaks from (00c) planes, among which the (001) peak shows the highest intensity. The broad diffraction peaks of SNO nanosheets to some extent suggest the decrease of crystal size after exfoliation, which is in agreement with the SEM images. In addition, the broad reflections located at ≈14° and ≈21° might result from nanosheet–water interface scattering, which was also observed in similar $Ca_2Nb_3O_{10}$ nanosheets.[29]

The morphology, crystalline phase, and elemental composition of SNO nanosheets are further characterized by transmission electron microscopy (TEM). According to Figure 2d, exfoliated SNO nanosheets with micrometer lateral size are observed by low-resolution TEM. The high-resolution TEM (HRTEM) image in Figure 2e illustrates the interplanar spacing of 0.38 nm along the two perpendicular directions, corresponding to (100) and (010) planes of SNO. The clear diffraction spots in selected area electron diffraction (SAED) pattern prove the high crystallization quality of SNO nanosheets, and the marked spots are indexed as (100) and (010) planes, respectively, suggesting the zone axis as [001]. The structural

information of SNO nanosheets by TEM is consistent with the XRD results. Furthermore, Figure 2g shows the structural illustration of SNO nanosheets, where three NbO_6 octahedral slabs share corners to form a unilamellar SNO nanosheet. The c-axis in Figure 2g is equivalent to the [001] zone axis in Figure 2f. In addition, the corresponding energy-dispersive X-ray spectroscopy (EDS) mapping images (Figure S4, Supporting Information) show the uniform distribution of elements. And the surface elemental composition and chemical state of SNO nanosheets are determined by X-ray photoelectron spectroscopy (XPS) (Figure S5, Supporting Information).

The optical properties are characterized by multiple techniques for a better insight into SNO nanosheets. According to the UV–vis absorption spectrum (Figure 2h), the sample shows negligible absorption over visible range and a sharp absorption edge at 300 nm, with its optical bandgap estimated to be 3.90 eV by the Tauc plot.[23] The high transparency of SNO sheets over the visible range (Figure S6, Supporting Information) indicates their potential for transparent UV-responsive devices. As is shown in Figure 2i, the room-temperature PL emission spectrum could be fitted into four bands by the Gaussian fit method. The PL peaks at 375 and 430 nm may be related to the band-to-band recombination and bound exciton recombination in SNO nanosheets, respectively. According to previous reports, the PL peak at ≈460 nm possibly originates from intrinsic NbO_6 groups, while the peak at 514 nm is ascribed to extrinsic NbO_6 groups, such as oxygen deficiencies.[30,31] Furthermore, the time-resolved photoluminescence (TRPL) spectrum is utilized

to determine the lifetime and dynamics of photogenerated carriers in SNO. Three time constants of 0.6, 6.6, and 36.0 ns are concluded from the triexponential fitting curve, and the average lifetime is calculated to be 0.81 ns. The fast PL decay process with the time constant of 0.6 ns could be related to free carrier recombination, and the other two longer time constants may be attributed to the formation and subsequent radiative annihilation of bound excitons. These processes are consistent with the corresponding bands in the PL spectrum. Moreover, the relationship between PL peaks and temperature is investigated by temperature-dependent PL measurement, and the exciton binding energy of SNO is estimated accordingly (Figure S7, Supporting Information). As the photoluminescent mechanisms in 2D perovskites are quite complex, further study is still in need to understand the photoluminescent properties in detail.

In order to investigate the photodetecting performance of SNO nanosheets, PDs based on individual few-layer SNO nanosheets are fabricated and characterized. **Figure 3**a shows

the AFM image of a typical SNO sheet–based PD (12.3 nm, 7L) with two Cr/Au contacts. It could be observed via *I–V* curves that the PD yields a low dark current of 2.1 pA at 1.0 V bias and a photocurrent up to 28.0 nA under 270 nm illumination. The high on/off ratio over 10^4 indicates that the SNO PD responds effectively to incident UV light. The spectral response of SNO is further investigated by varying incident wavelength, and the spectral responsivity (R_λ), EQE, and specific detectivity (D^*) are crucial figures of merit for performance evaluation[32]

$$R_\lambda = (I_p - I_d)/P_\lambda S \tag{1}$$

$$EQE = R_\lambda hc/e\lambda \tag{2}$$

$$D^* = R_\lambda (2eI_d/S)^{-1/2} \tag{3}$$

where I_p and I_d are photocurrent and dark current, P_λ is the incident power density, S is the effective exposure area, and *h*, *c*, *e*,
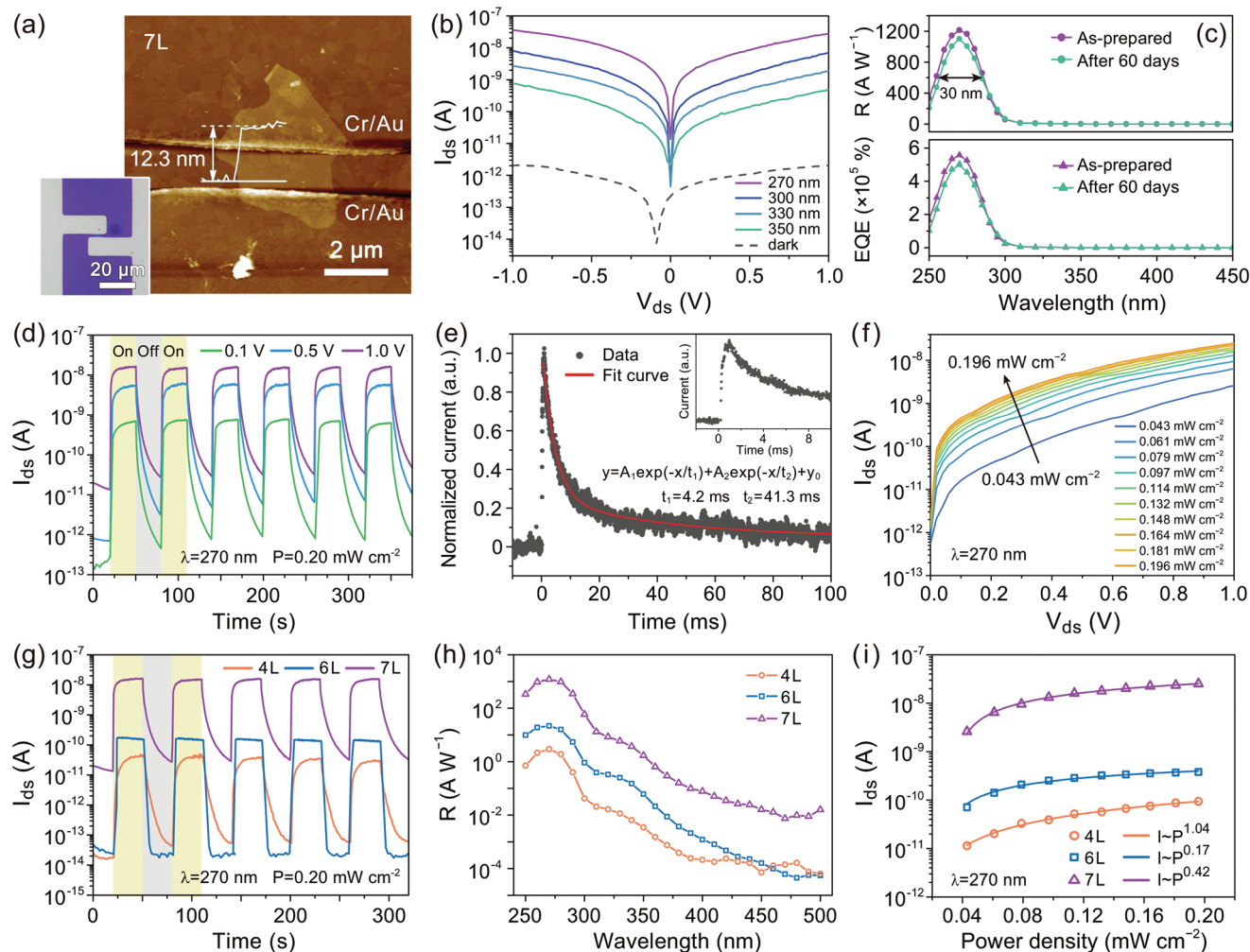

Figure 3. Photodetecting performance of individual few-layer SNO nanosheets. a) The AFM image of a 7L SNO PD, with the optical image shown in the inset. b) The semi-logarithmic *I–V* curves of 7L SNO under dark and UV illumination. c) The spectral responsivity and EQE of 7L SNO PD at 1 V bias, as-prepared, and after 60 days in ambient condition. d) *I–t* curves of 7L SNO under 270 nm UV on/off switching at various bias voltages. e) The pulse response of 7L SNO PD at 1 V bias with the extracted time constants. The rising edge of pulse response is shown in the inset. f) *I–V* curves of 7L SNO under various incident power densities. g) *I–t* curves of SNO nanosheets with various thicknesses (4L, 6L, and 7L) at 1 V bias. h) The responsivity of SNO nanosheets with various thicknesses at 1 V bias. i) Photocurrent as a function of incident power density and their corresponding power fits at 1 V bias.

and λ are Planck's constant, the velocity of light, the elementary charge, and incident wavelength, respectively. According to Figure 3c, the SNO PD exhibits outstanding UV photodetecting performance, including an excellent responsivity of 1214 A W^{-1} and a high EQE of 5.6×10^5% under 270 nm illumination (0.20 mW cm^{-2}) at 1.0 V bias. Here the high EQE value may be a result of hole-trapping effect by surface oxygen adsorption, which prolongs the photogenerated electron lifetime and reduced carrier transit time between two metal contacts with a short separation ($\approx$1.5 μm).[33] And the PD shows a high detectivity of 1.4×10^{14} Jones under 270 nm illumination (Figure S11a, Supporting Information), proving its capacity for detecting signal from noise environment. Besides, the PD shows a narrowband responsivity with a full-width at half-maximum (FWHM) of 30 nm, enabling specific wavelength photodetection. The excellent responsivity at a narrow UV range shows the potential of SNO as a promising candidate for narrowband solar-blind UV PDs, outperforming most reported 2D material–based UV PDs (Table S3, Supporting Information). The cutoff wavelengths at $\approx$310 nm correspond with the optical bandgap measured by UV–vis spectra (Figure 2h). Moreover, the SNO PD exhibits high stability under ambient condition, with only a slight reduction in R_λ and EQE after 60 days without any treatment (Figure 3c). Figure 3d illustrates the time-resolved current (I–t) under 270 nm UV on/off switching, and the SNO PD shows fast response speed and high repeatability to UV switching at various bias voltages. The PD yields a stable I_p of 15.5 nA at 1.0 V bias, and an I_p of 0.7 nA could be obtained at a bias as low as 0.1 V. To further investigate the response time of the device, pulse response performance is characterized with a pulsed laser source (Figure 3e). It is estimated that the rise time (t_{rise}) and decay time (t_{decay}) of the 7L device under laser pulse are 0.4 and 40 ms, respectively. And the two time constants extracted by second-order exponential fitting of the decay curve are 4.2 and 41.3 ms, respectively, suggesting its outstanding response speed. Interestingly, compared with the TRPL decay curve above, the pulse response of the SNO PD shows a much longer decay process, implying the dominant effect of nonradiative recombination in SNO sheets after removing the incident light. Moreover, when tested in vacuum, the PD yields improved I_p as high as 1 μA at 1.0 V bias and shows 16.2 times the R_λ of that tested in ambient pressure, while the response time is greatly prolonged (Figure S8, Supporting Information). This phenomenon could be related to the increased carrier number in vacuum condition where the effect of surface oxygen adsorption is eliminated.[34]

The thickness-dependent properties of 2D materials are of great importance for the investigation and exploitation of those atomically thin materials. Herein, the UV photodetecting performance of individual SNO nanosheets with various layer numbers (4L, 6L, and 7L) is investigated and summarized (Figure 3; Figures S9–S11, Supporting Information). Due to the difficulty of exfoliating and dispersing SNO nanosheets, with both large size and atomically thin thickness, on substrates for subsequent device fabrication, SNO PDs with thicknesses below 4L are not investigated in this work. As is shown in Figure 3g, the I–t curves of the fabricated SNO PDs at 1 V bias show fast response speed and high repeatability toward 270 nm UV on/off switching. It is observed that the photocurrent value

increases with the increase of SNO layer number, while SNO PDs with lower thicknesses have an advantage of extremely low dark current ($\approx$10^{-14} A). According to R_λ curves in Figure 3h, all the SNO PDs exhibit obvious cutoff edges at $\approx$310 nm with their highest R_λ located at 270 nm, indicating that the PDs share similar bandgap corresponding to the UV region. The cutoff edges (310 nm) are consistent with the optical bandgap value measured by UV–vis spectroscopy in Figure 2h (3.9 eV). And it is noteworthy that all the SNO PDs show narrowband responsivity, with FWHM values of 26, 32, 30 nm for 4L, 6L, and 7L PDs, respectively. Besides, the thickness dependence of R_λ is also observed, with the 7L PD showing the highest responsivity, followed by that of 6L and 4L. The higher R_λ of thicker nanosheets in part results from their higher UV absorption compared with those with smaller thicknesses.[35] And previous reports have developed a resistor network model to explain the relationship between the resistance of 2D nanosheets and their thickness. That is, to some extent, the resistance of nanosheets is reduced with the increase of their thickness, which could also lead to higher photocurrent and thus improved R_λ.[36] The two factors, along with the carrier mobility discussed later, are possible causes that contribute to the thickness dependence of R_λ. More figures of merit of SNO PDs with various thicknesses, including D^* and EQE, are available in Figure S11 (Supporting Information). Furthermore, the relationship between photocurrent of SNO PDs and incident power density is investigated, and the plots in Figure 3i could be well fitted by the power-law relationship, $I_p \approx P^a$. The exponent a for 4L PD is close to 1, indicating its near-linear dependence, while 6L and 7L PDs show sublinear relationship ($a < 1$). According to previous studies, a relatively low value of a denotes high density of surface carrier traps.[32,37] It is natural that liquid-exfoliated nanosheets abound in defects and surface traps, which may contribute to an increased photoconductive gain.[33] And because of the high surface-to-volume ratio of 2D nanosheets, surface defects and traps may provide abundant recombination centers, which contributes to the fast decay speed of the PDs when UV light is switched off.[38,39] In general, few-layer SNO nanosheets exhibit outstanding and thickness-dependent UV photodetecting performance, proving SNO a promising candidate for high-performance UV PDs.

With the aim of getting insightful understanding and further controlling the carrier transport properties of SNO, SNO nanosheet–based back-gate field-effect transistors (FETs) are fabricated on heavily doped Si substrate with an oxidation layer and characterized by three-terminal measurements. As is shown in **Figure 4**b, the transfer characteristics of SNO with various thicknesses suggest the n-type nature of SNO. And the threshold voltages for electron conduction of 4L, 6L, and 7L SNO transistors are measured to be 3.6, 5.4, and 8.5 V, respectively, showing an increasing trend with increasing nanosheet thickness. According to transfer curves, the field-effect carrier mobility (μ_{FE}) could be extracted as follows[36]

$$\mu_{FE} = \frac{dI_{ds}}{dV_{gs}} \times \frac{L}{W V_{ds} C_{ox}} \qquad (4)$$

where L and W are channel length and width, and C_{ox} is the oxide layer capacitance per unit area (1.2×10^{-8} F cm^{-2}

**ADVANCED
SCIENCE NEWS**

www.advancedsciencenews.com
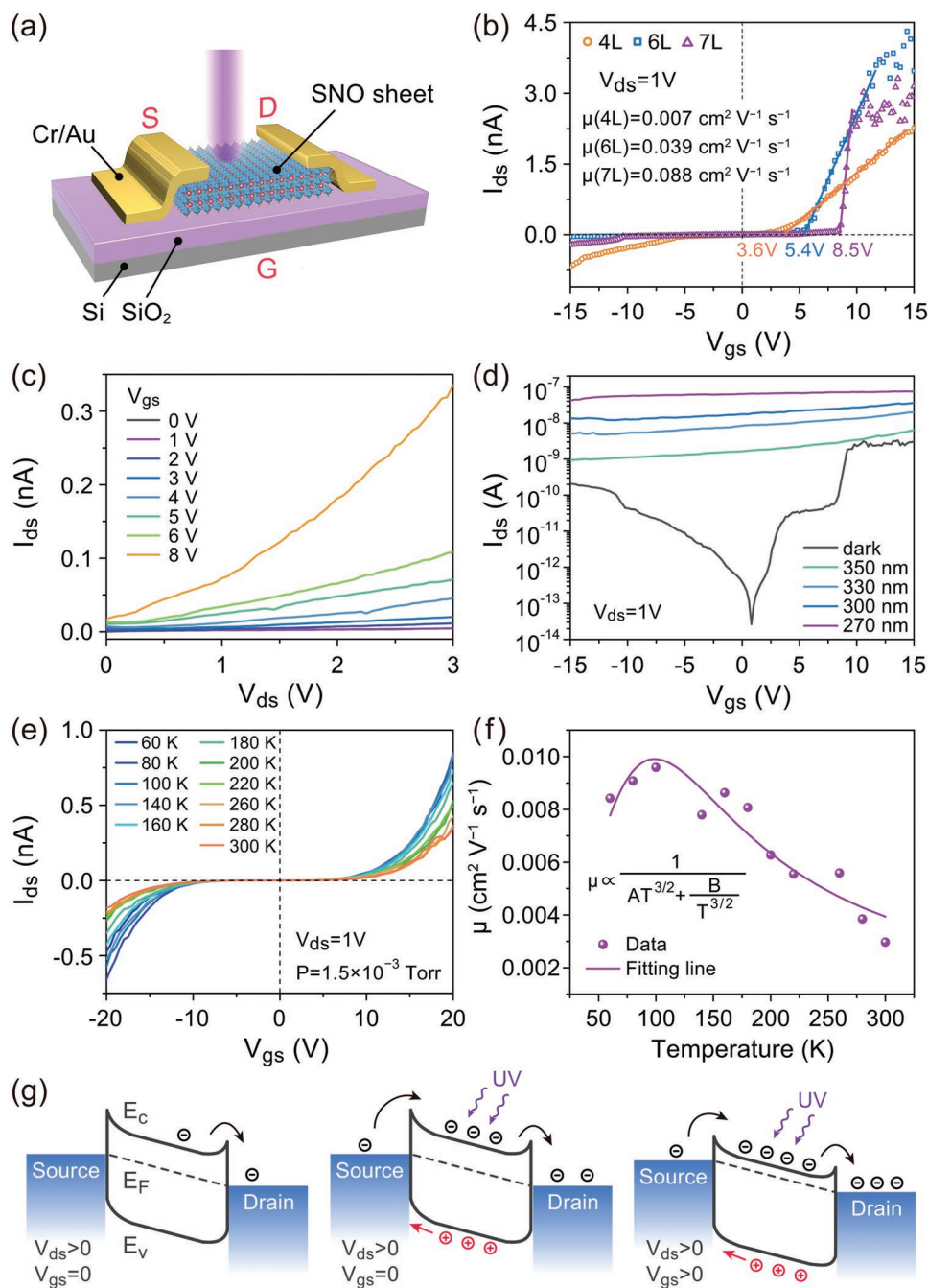
**ADVANCED
MATERIALS**

www.advmat.de

Figure 4. The illustration and performance of SNO nanosheet–based phototransistors. a) The schematic illustration of fabricated phototransistors based on individual few-layer SNO nanosheets. b) The transfer characteristics of SNO transistors with various thicknesses in dark condition. Field-effect carrier mobility is extracted. c) The output characteristics of the 7L SNO transistor in dark condition. d) Phototransistor performance of 7L SNO at dark and under UV illumination, at V_{ds} = 1 V. The temperature-dependent e) transfer curves and f) field-effect carrier (electrons) mobility of the 7L SNO transistor. g) The band diagrams of SNO transistors under different conditions.

for 300 nm SiO_2). It is found that with the layer number decreasing, the μ_{FE} of SNO decreases from 0.088 cm^2 V^{-1} s^{-1} for 7L SNO to 0.039 and 0.007 cm^2 V^{-1} s^{-1} for 6L and 4L SNO, respectively. The declined μ_{FE} with a decreased layer number could be explained by dominant interfacial impurities in atomically thin channels.[36,40] In addition, the output characteristics of SNO FET (Figure 4c) prove that the I_{ds} could be

effectively modulated by the gate voltage, where I_{ds} shows an obvious increase with the positive shift of V_{gs}. Furthermore, according to the semi-logarithmic transfer curve in dark condition (Figure 4d), the SNO FET exhibits an ambipolar behavior that electron and hole conduction could both be modulated by applied V_{gs}. The on/off ratios for electron accumulation and hole accumulation are measured to be over 10^5 and 8×10^3,

**ADVANCED
SCIENCE NEWS**

www.advancedsciencenews.com

**ADVANCED
MATERIALS**

www.advmat.de

respectively. By contrast, when under UV illumination, no ambipolar behavior is observed in the SNO FET, and the I_{ds} is less dependent on the V_{gs} compared with that in dark, although the photocurrent could be further enhanced by the positive shift of V_{gs}. Under 270 nm UV illumination, the I_{ds} reaches its maximum as high as 75 nA at $V_{gs} = 15$ V.

To better understand the temperature-dependent carrier transport properties, the low-temperature transfer characteristic of the SNO transistor is investigated from 60 to 300 K in vacuum. And the result suggests that with lowering temperature, the I_{ds} of 7L SNO increases and then decreases after reaching the maximum at the temperature of 100 K. Based on the transfer curves, the temperature dependence of μ_{FE} could be extracted (Figure 4f). It is found that the μ_{FE} depends strongly on the temperature in a nonmonotonic way, with its maximum located at about 100 K. Similar temperature-dependent mobility results were observed in some other 2D materials.[41,42] This nonlinear μ_{FE} versus T relationship could be explained by two co-existing carrier scattering mechanisms in SNO nanosheets, which have a great effect on the mean free time of carriers and, consequently, on the carrier mobility. According to previous studies, the temperature dependence of μ_{FE} dominated by both phonon and impurity scattering is expressed as follows[43,44]

$$\mu_{FE} \propto \frac{1}{AT^{3/2} + \dfrac{B}{T^{3/2}}} \qquad (5)$$

where A and B are coefficients related to phonon scattering and impurity scattering, respectively. With the equation, the μ_{FE} versus T data points can be well fitted, to some extent validating the proposed scattering mechanism of carriers in SNO nanosheets. That is, the carrier transport is dominated by impurity scattering at low temperature (<100 K), and is limited mainly by phonon scattering at higher temperature as thermal vibration increases.[41] It is noteworthy that the measured μ_{FE} in Figure 4e is lower than that in Figure 4b (in the air), which may be attributed to the increased oxygen defects' scattering in vacuum environment when conducting low-temperature measurements.

The proposed band diagrams of SNO PDs under different circumstances are shown in Figure 4g. In dark conditions, SNO PDs are in an equilibrium state with small Schottky barriers at the electrode contacts. When external V_{ds} is applied, electrons transport from source to drain according to thermionic and tunneling mechanisms, forming a relatively low dark current. As for SNO-based transistors, the dark current could be effectively modulated by modifying the V_{gs}. Under UV illumination, a great number of photogenerated electron–hole pairs in SNO are effectively separated by external V_{ds}, contributing greatly to the photocurrent. As gate voltage–induced carriers are heavily outnumbered by photogenerated ones, the photoelectric effect dominates over the thermionic and tunneling mechanisms in photocurrent, leading to a dramatically enhanced and less V_{gs}-dependent photocurrent. By positively increasing the V_{gs}, the contact barriers can be lowered, resulting in a further increased I_{ds}. When UV light is switched off, rapid recombination of photogenerated carrier

pairs occurs at abundant recombination centers in SNO nanosheets, which contributes to the fast decay speed as discussed above.

Nowadays, optoelectronic devices with transparent and flexible features have seen rapid development. Here, flexible SNO film PDs with centimeter scale are easily constructed on polyethylene terephthalate (PET) substrate by a facile drop-coating approach without any extra additive. The channel length between two Cr/Au contacts is kept at 1 mm. Prior to the bending test, the flexible PD exhibits a dark current of 4.7 nA at 1 V bias, and yields the I_p of 1.6 μA under 300 nm UV illumination (0.39 mW cm^{-2}), as is shown in **Figure 5**b. The R_λ and EQE curves show clear cutoff edges at the wavelength of 350 nm with their maximum values located at 300 nm. The slight redshift of maximum R_λ and EQE value compared with that of individual nanosheet devices above (270 nm) might be a consequence of decreased bandgap due to increased film thickness. During the bending test, the flexible PD could stand up to the bending angle up to 80° with the I_p remaining almost unchanged. It is observed that the I_d shows a declining tendency with the increase of bending angle, resulting in an increasing on/off ratio when the bending angle is below 80° (Figure 5f). The declined I_d may result from the improved resistance between SNO nanosheets due to tiny cracks formed during the bending test. In addition, we investigated the variation of photodetecting performance after certain cycles of repeated bending test, with the illustration of one bending cycle shown in Figure S13 (Supporting Information). As is shown in Figure 5g,h, the I_p and R show a rapid declination in the first 100 cycles and subsequently level off before a sudden drop after around 900 cycles. According to the optical images in Figure S14 (Supporting Information), the evolution of performance is closely related to the initiation and propagation of cracks in SNO sheet film, and after hundreds of bending cycles, those cracks eventually lead to device failure. Considering the simple, additive-free, drop-coating fabrication process of the flexible PD, the performance in bending tests is quite satisfactory and could be further improved in future study. In brief, the successful fabrication of SNO flexible PDs shows the potential of forming SNO sheet–based film on other flexible substrates by other practical solution-based methods, such as spin coating, spraying, and self-assembly, toward further enhanced performance in future study.

In summary, 2D perovskite SNO nanosheets with thicknesses down to 1.8 nm are synthesized via liquid exfoliation of precursor CSNO prepared by a two-step high-temperature solid state reaction. XRD and TEM results suggest high crystallinity of prepared SNO nanosheets. The room-temperature PL and TRPL spectra reveal complicated radiative recombination mechanisms in SNO nanosheets. By fabricating UV PDs based on individual few-layer SNO sheets, it is found that exfoliated SNO nanosheets exhibit outstanding performance, including an excellent narrowband responsivity over 1200 A W^{-1}, an EQE of 5.6×10^5%, a detectivity of 1.4×10^{14} Jones (7L SNO, 270 nm, 1 V bias), as well as fast response speed ($t_{rise} \approx 0.4$ ms, $t_{decay} \approx 40$ ms), outperforming most of reported 2D material–based UV PDs. More intriguingly, SNO sheets with greater thicknesses show a higher value of photocurrent
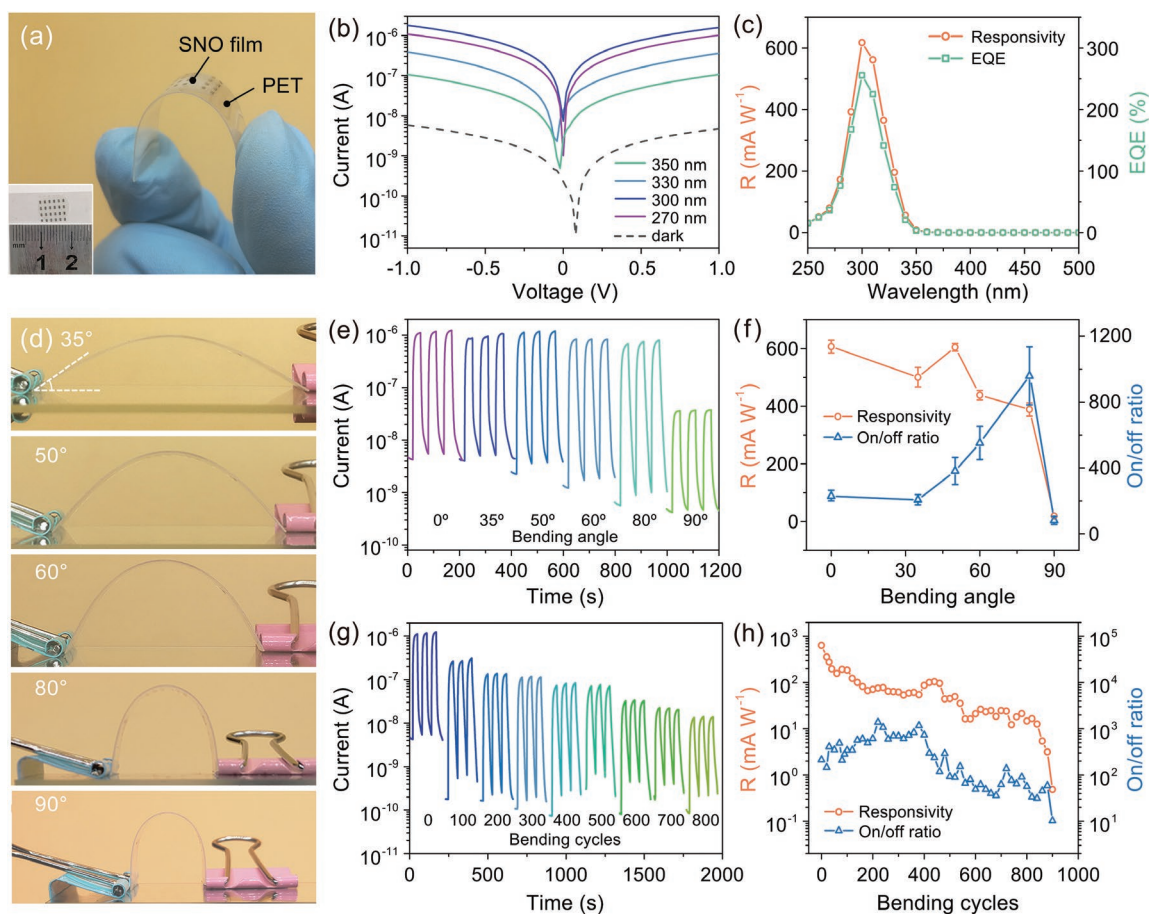
**ADVANCED
SCIENCE NEWS**

www.advancedsciencenews.com

**ADVANCED
MATERIALS**

www.advmat.de

Figure 5. Photodetecting performance of flexible PDs based on SNO nanosheet film. a) The optical image of a flexible SNO PD on PET substrate. b) The I–V curves of a flexible SNO PD in dark and under UV illumination. c) The R_λ (orange line) and EQE (green line) at 1 V bias. d) The illustration of the bending test. e) The I–t curves under 300 nm UV switching (0.39 mW cm^{-2}) at 1 V bias, measured at various bending angles. f) The variation of R_λ and on/off ratio with the bending angle. g) The I–t curves under 300 nm UV switching at 1 V bias, measured after every 100 bending cycles. h) The variation of R_λ and on/off ratio with increasing bending cycles.

and photoresponsivity under UV illumination, indicating the thickness dependence of SNO photodetecting performance. The high photodetecting performance of SNO nanosheets lies in their high crystallinity during high-temperature synthesis, and defects formed during the fabrication process contribute to the high photoconductive gain. Furthermore, in SNO transistors, the field-effect mobility of SNO sheets with various thicknesses are extracted, and the carrier transport properties of SNO sheets could be easily modulated by applying a gate voltage. Under UV illumination, photogenerated electron–hole pairs outnumber thermionic and tunneling carriers, resulting in a greatly improved photocurrent in SNO phototransistors. By conducting low-temperature mobility tests, we deduced that phonon scattering and impurity scattering coexist in SNO sheets. In addition, flexible and transparent PDs based on SNO nanosheet film via an easy and low-cost drop-coating process show satisfactory responsivity and can keep their performance in repeated bending tests. This work not only suggests the high performance of 2D perovskite SNO PDs, but also sheds light on the development of high-performance optoelectronics based on stable low-dimensional wide-bandgap perovskites in the future.

Experimental Section

Synthesis of Sr₂Nb₃O₁₀ Nanosheets: The synthesis process was carried out as previously reported with modification.[22,23] Briefly, Cs_2CO_3 (99.99%), $SrCO_3$ (99.9%), and Nb_2O_5 (99.99%) with the molar ratio of Cs:Sr:Nb = 1.2:2:3 were mixed thoroughly by grinding the mixture for 0.5 h before calcinated at 1100 °C for 10 h in air. After that, 5 mol% Cs_2CO_3 was added into the calcinated product and ground thoroughly before second calcination at 1350 °C for 10 h in air. For each step, the excess amount of Cs_2CO_3 compensated for its loss at high temperature. After calcination, Cs^+ was replaced with H^+ by slowly stirring 0.5 g of obtained powder with 20 mL of 2 M HCl for 4 days during which acid was renewed daily. The powder was then washed thoroughly with distilled water and dried at 80 °C in air, and 0.2 g of HSNO powder was dispersed in 50 mL of aqueous solution containing an equimolar amount of TBAOH (prepared from 25% aqueous solution). The SNO nanosheets were prepared by shaking the TBAOH-containing solution under room temperature for 10 days, then washed three times with distilled water and collected by centrifugation. Before any characterization and measurement, (TBA)SNO sheets were dispersed on substrates and then kept under UV exposure to burn out residual TBA^+.[29]

Characterization of SNO Samples: The size and morphology of exfoliated SNO nanosheets were investigated by field-emission SEM (Zeiss Sigma). The AFM measurement was conducted on a Bruker Dimension Edge atomic force microscope. High-resolution morphology

and structure of SNO nanosheets were characterized by TEM (JOEL JEM-2100F). A Bruker D8-A25 diffractometer was used for the crystal structure analysis of powder samples using Cu Kα radiation (λ = 1.5405 Å), while GIXRD was performed for SNO nanosheets on a Rigaku Smartlab9 diffractometer. The XPS test was carried out using a PHI 5300 ESCA system (Mg, 14 kV, 250 W). UV–vis spectra were obtained by measuring dispersed SNO nanosheets on quartz substrate using a UV–vis spectrophotometer (Hitachi U-3900H). The room-temperature PL and TRPL emission spectra were obtained on an Edinburgh FS5 spectrofluorometer. Temperature-dependent PL emission spectra were measured by a LabRAM HR800 spectrometer (HORIBA Jobin Yvon).

Photoelectric Measurements: The SNO-based PDs on Si/SiO$_2$ substrate were fabricated by photolithography, electron beam deposition of metal contacts (15/50 nm Cr/Au), and subsequent lift-off process. The photolithography was conducted on a Heidelberg µPG 501 direct writer system. After lift-off, fabricated devices were annealed at 200 °C in Ar atmosphere for 2 h. For the construction of flexible SNO PDs, a shadow mask was used for patterning of Cr/Au contacts. All the electric and photoelectric measurements were conducted using a semiconductor characterization system (Keithley 4200, USA) and a four-probe station. A 450 W Xenon lamp equipped with a monochromator was utilized as the light source whose power density was measured with a NOVA II power meter (OPHIR Photonics). For pulse response characterization, a digital oscilloscope (Tektronix DPO 5140B) and a 355 nm Nd:YAG pulsed laser system with a pulse duration of 3–5 ns were used. Temperature-dependent transport properties were measured using a closed-cycle helium compressor-cooled cryostat (HC-4E1, Sumitomo).

Supporting Information

Supporting Information is available from the Wiley Online Library or from the author.

Conflict of Interest

The authors declare no conflict of interest.

Keywords

[1] S. Cai, X. J. Xu, W. Yang, J. X. Chen, X. S. Fang, *Adv. Mater.* **2019**, *31*, 1808183.
[2] V. Adinolfi, O. Ouellette, M. I. Saidaminov, G. Walters, A. L. Abdelhady, O. M. Bakr, E. H. Sargent, *Adv. Mater.* **2016**, *28*, 7264.
[3] W.-Y. Kong, G.-A. Wu, K.-Y. Wang, T.-F. Zhang, Y.-F. Zou, D.-D. Wang, L.-B. Luo, *Adv. Mater.* **2016**, *28*, 10725.
[4] X. J. Xu, S. Li, J. Chen, S. Cai, Z. Long, X. S. Fang, *Adv. Funct. Mater.* **2018**, *28*, 1802029.
[5] F. H. L. Koppens, T. Mueller, P. Avouris, A. C. Ferrari, M. S. Vitiello, M. Polini, *Nat. Nanotechnol.* **2014**, *9*, 780.
[6] Y. Zhang, W. X. Xu, X. J. Xu, J. Cai, W. Yang, X. S. Fang, *J. Phys. Chem. Lett.* **2019**, *10*, 836.
[7] H. Tsai, W. Nie, J.-C. Blancon, C. C. Stoumpos, R. Asadpour, B. Harutyunyan, A. J. Neukirch, R. Verduzco, J. J. Crochet, S. Tretiak, L. Pedesseau, J. Even, M. A. Alam, G. Gupta, J. Lou, P. M. Ajayan, M. J. Bedzyk, M. G. Kanatzidis, A. D. Mohite, *Nature* **2016**, *536*, 312.
[8] J. Xing, Y. Zhao, M. Askerka, L. N. Quan, X. Gong, W. Zhao, J. Zhao, H. Tan, G. Long, L. Gao, Z. Yang, O. Voznyy, J. Tang, Z.-H. Lu, Q. Xiong, E. H. Sargent, *Nat. Commun.* **2018**, *9*, 3541.
[9] P. Li, Y. Chen, T. Yang, Z. Wang, H. Lin, Y. Xu, L. Li, H. Mu, B. N. Shivananju, Y. Zhang, Q. Zhang, A. Pan, S. Li, D. Tang, B. Jia, H. Zhang, Q. Bao, *ACS Appl. Mater. Interfaces* **2017**, *9*, 12759.
[10] X. Qi, Y. Zhang, Q. Ou, S. T. Ha, C.-W. Qiu, H. Zhang, Y.-B. Cheng, Q. Xiong, Q. Bao, *Small* **2018**, *14*, 1800682.
[11] D. Li, G. Wang, H.-C. Cheng, C.-Y. Chen, H. Wu, Y. Liu, Y. Huang, X. Duan, *Nat. Commun.* **2016**, *7*, 11330.
[12] Y.-Q. Zhao, Q.-R. Ma, B. Liu, Z.-L. Yu, J. Yang, M.-Q. Cai, *Nanoscale* **2018**, *10*, 8677.
[13] Z. Wu, C. Ji, L. Li, J. Kong, Z. Sun, S. Zhao, S. Wang, M. Hong, J. Luo, *Angew. Chem., Int. Ed.* **2018**, *57*, 8140.
[14] H.-C. Cheng, G. Wang, D. Li, Q. He, A. Yin, Y. Liu, H. Wu, M. Ding, Y. Huang, X. Duan, *Nano Lett.* **2016**, *16*, 367.
[15] B.-W. Li, M. Osada, Y. Ebina, S. Ueda, T. Sasaki, *J. Am. Chem. Soc.* **2016**, *138*, 7621.
[16] K. Maeda, G. Sahara, M. Eguchi, O. Ishitani, *ACS Catal.* **2015**, *5*, 1700.
[17] X. Yang, X. Zhang, J. Deng, Z. Chu, Q. Jiang, J. Meng, P. Wang, L. Zhang, Z. Yin, J. You, *Nat. Commun.* **2018**, *9*, 570.
[18] K.-T. Ho, S.-F. Leung, T.-Y. Li, P. Maity, B. Cheng, H.-C. Fu, O. F. Mohammed, J.-H. He, *Adv. Mater.* **2018**, *30*, 1804372.
[19] X. Hu, X. Zhang, L. Liang, J. Bao, S. Li, W. Yang, Y. Xie, *Adv. Funct. Mater.* **2014**, *24*, 7373.
[20] Y. Zhang, J. Liu, Z. Wang, Y. Xue, Q. Ou, L. Polavarapu, J. Zheng, X. Qi, Q. Bao, *Chem. Commun.* **2016**, *52*, 13637.
[21] M. Osada, T. Sasaki, *Adv. Mater.* **2012**, *24*, 210.
[22] W.-H. Lee, M. Im, S.-H. Kweon, J.-U. Woo, S. Nahm, J.-W. Choi, S.-J. Hwang, *J. Am. Ceram. Soc.* **2017**, *100*, 1098.
[23] P. Xu, T. J. Milstein, T. E. Mallouk, *ACS Appl. Mater. Interfaces* **2016**, *8*, 11539.
[24] D. Ji, S. Cai, T. R. Paudel, H. Sun, C. Zhang, L. Han, Y. Wei, Y. Zang, M. Gu, Y. Zhang, W. Gao, H. Huyan, W. Guo, D. Wu, Z. Gu, E. Y. Tsymbal, P. Wang, Y. Nie, X. Pan, *Nature* **2019**, *570*, 87.
[25] K. Maeda, M. Eguchi, T. Oshima, *Angew. Chem., Int. Ed.* **2014**, *53*, 13164.
[26] K. Domen, J. Yoshimura, T. Sekine, A. Tanaka, T. Onishi, *Catal. Lett.* **1990**, *4*, 339.
[27] Z. Zhong, W. Ding, W. Hou, Y. Chen, X. Chen, Y. Zhu, N. Min, *Chem. Mater.* **2001**, *13*, 538.
[28] K. Okamoto, H. Sato, K. Saruwatari, K. Tamura, J. Kameda, T. Kogure, Y. Umemura, A. Yamagishi, *J. Phys. Chem. C* **2007**, *111*, 12827.
[29] S.-H. Kweon, M. Im, W.-H. Lee, S. Nahm, J.-W. Choi, S.-J. Hwang, *J. Mater. Chem. C* **2016**, *4*, 178.
[30] G. Blasse, L. H. Brixner, *Mater. Res. Bull.* **1989**, *24*, 363.
[31] M. Wiegel, M. Hamoumi, G. Blasse, *Mater. Chem. Phys.* **1994**, *36*, 289.
[32] W. X. Ouyang, F. Teng, X. S. Fang, *Adv. Funct. Mater.* **2018**, *28*, 1707178.

[33] L. F. Hu, J. Yan, M. Liao, L. Wu, X. S. Fang, *Small* **2011**, *7*, 1012.

[34] H. Liu, Z. Zhang, L. Hu, N. Gao, L. Sang, M. Liao, R. Ma, F. Xu, X. S. Fang, *Adv. Opt. Mater.* **2014**, *2*, 771.

[35] W. Feng, J.-B. Wu, X. Li, W. Zheng, X. Zhou, K. Xiao, W. Cao, B. Yang, J.-C. Idrobo, L. Basile, W. Tian, P. Tan, P. Hu, *J. Mater. Chem. C* **2015**, *3*, 7022.

[36] S. Das, H.-Y. Chen, A. V. Penumatcha, J. Appenzeller, *Nano Lett.* **2013**, *13*, 100.

[37] F. Wang, T. Gao, Q. Zhang, Z.-Y. Hu, B. Jin, L. Li, X. Zhou, H. Li, G. Van Tendeloo, T. Zhai, *Adv. Mater.* **2019**, *31*, 1806306.

[38] G. Cunningham, D. Hanlon, N. McEvoy, G. S. Duesberg, J. N. Coleman, *Nanoscale* **2015**, *7*, 198.

[39] X. Zhou, Q. Zhang, L. Gan, H. Li, T. Zhai, *Adv. Funct. Mater.* **2016**, *26*, 4405.

[40] S.-L. Li, K. Wakabayashi, Y. Xu, S. Nakaharai, K. Komatsu, W.-W. Li, Y.-F. Lin, A. Aparecido-Ferreira, K. Tsukagoshi, *Nano Lett.* **2013**, *13*, 3546.

[41] S. Kim, A. Konar, W.-S. Hwang, J. H. Lee, J. Lee, J. Yang, C. Jung, H. Kim, J.-B. Yoo, J.-Y. Choi, Y. W. Jin, S. Y. Lee, D. Jena, W. Choi, K. Kim, *Nat. Commun.* **2012**, *3*, 1011.

[42] X. Y. Chin, D. Cortecchia, J. Yin, A. Bruno, C. Soci, *Nat. Commun.* **2015**, *6*, 7383.

[43] Z.-Y. Ong, M. V. Fischetti, *Phys. Rev. B* **2013**, *88*, 165316.

[44] H. T. Yi, X. Wu, X. Zhu, V. Podzorov, *Adv. Mater.* **2016**, *28*, 6509.